

DCT-Mamba3D: Spectral Decorrelation and Spatial-Spectral Feature Extraction for Hyperspectral Image Classification

WeiJia Cao¹ Xiaofei Yang² Yicong Zhou³ Zheng Zhang⁴

¹Aerospace Information Research Institute, Chinese Academy of Sciences, Beijing, China

²Guangzhou University, Guangzhou, China

³University of Macau, Macau, China

⁴Harbin Institute of Technology, Shenzhen, China

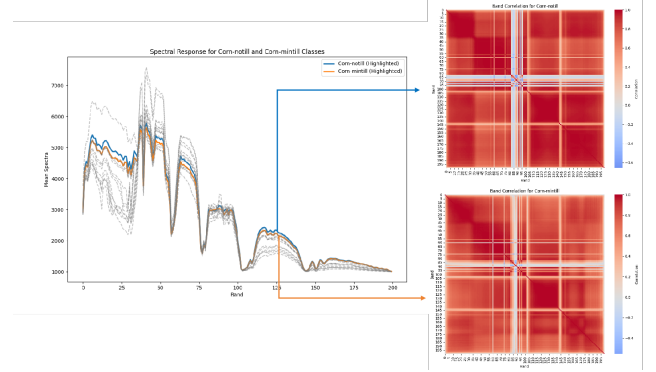
caowj@aircas.ac.cn, xiaofei yang@gzhu.edu.cn, yicongzhou@um.edu.mo, darrenzz219@gmail.com

Abstract

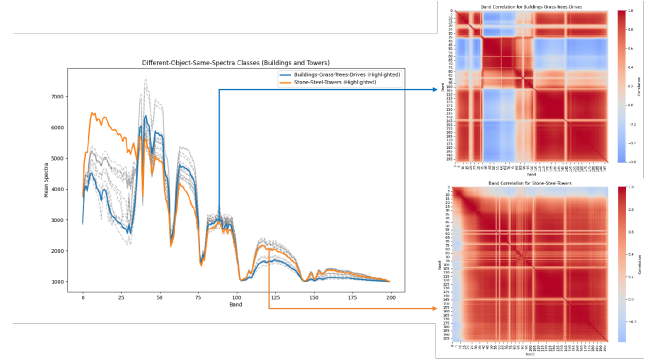
Hyperspectral image classification presents challenges due to spectral redundancy and complex spatial-spectral dependencies. This paper proposes a novel framework, DCT-Mamba3D, for hyperspectral image classification. DCT-Mamba3D incorporates: (1) a 3D spectral-spatial decorrelation module that applies 3D discrete cosine transform basis functions to reduce both spectral and spatial redundancy, enhancing feature clarity across dimensions; (2) a 3D-Mamba module that leverages a bidirectional state-space model to capture intricate spatial-spectral dependencies; and (3) a global residual enhancement module that stabilizes feature representation, improving robustness and convergence. Extensive experiments on benchmark datasets show that our DCT-Mamba3D outperforms the state-of-the-art methods in challenging scenarios such as the same object in different spectra and different objects in the same spectra.

1. Introduction

Hyperspectral image (HSI) classification is crucial in remote sensing applications, such as environmental monitoring, agriculture, and mineral exploration [14, 34]. However, high dimensionality and spectral redundancy in HSI data—often termed the “curse of dimensionality”—pose unique challenges, complicating effective classification [8, 11]. This redundancy hampers performance, particularly in cases where different objects share similar spectra or the same object exhibits spectral variability under different conditions [21, 31]. Figure 1 illustrates these phenomena, emphasizing the need for methods that capture essential spatial-spectral features while reducing redundant information [5, 12].



(a) Same object, different spectra: Spectral variability in corn types (*Corn-notill* and *Corn-minill*). Highlighted curves represent specific types, while gray curves show other corn samples, reflecting intra-class variability influenced by spectral redundancy and high correlation.



(b) Different objects, same spectra: Spectral similarity between *Buildings-Grass-Trees-Drives* and *Stone-Steel-Towers*. Highlighted curves represent these classes, with gray curves showing other land cover types, illustrating inter-class similarity caused by spectral overlap and strong correlation.

Figure 1. Spectral response functions illustrating HSI classification challenges due to spectral redundancy and high correlation.

Challenges of Spectral Variability and Redundancy: Spectral variability (caused by changing illumination, at-

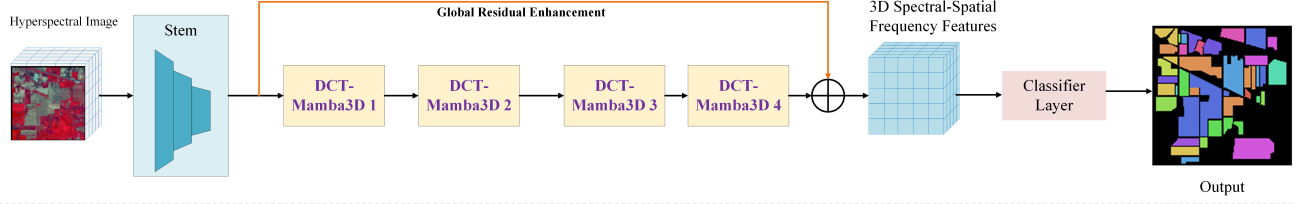


Figure 2. DCT-Mamba3D framework.

mospheric conditions, or intrinsic material differences) and similarity between materials exacerbate classification challenges [9, 21, 31]. High inter-band correlation leads to redundant information, complicating differentiation, particularly in mixed pixels where each pixel may represent multiple materials [3].

Frequency-Domain Transformations for Enhanced Feature Extraction: Frequency-domain transformations can improve spectral separation and feature extraction in HSI classification [15, 27]. Discrete cosine transform (DCT) specifically enables decorrelation by transforming data into the frequency domain, facilitating refined feature extraction [19, 22, 23, 26].

Recent approaches in HSI classification explore CNN-based, Transformer-based, and Mamba-based architectures. CNN-based methods, such as 2D-CNN [28], 3D-CNN [29], and HybridSN [16], primarily focus on spatial features but often overlook complex spectral correlations [4, 10, 23, 25]. Transformer-based models, including ViT [6], HiT [30], CAT [7], and MorphF [17], utilize self-attention mechanisms to capture spectral dependencies but are computationally intensive and often require large datasets [7,

18]. Mamba-based models, such as MiM [35], Spectral-Mamba [31], WaveMamba [1], and Vision Mamba [36], employ state-space representations to model spatial-spectral relationships without convolutional structures but face limitations in addressing spectral redundancy and inter-band correlation.

In this paper, we propose *DCT-Mamba3D*, an HSI classification model that integrates a 3D Spatial-Spectral Decorrelation Module (3D-SSDM), a 3D-Mamba module, and a Global Residual Enhancement (GRE) module to reduce spectral redundancy and enhance feature extraction. 3D-SSDM uses 3D DCT basis functions to transform data into the frequency domain, enabling both spectral and spatial decorrelation and improving feature clarity for subsequent extraction layers. The 3D-Mamba module leverages a 3D state-space model to capture intricate spatial-spectral dependencies. Finally, the GRE module stabilizes feature representation, enhancing robustness and convergence.

Our contributions are as follows:

- **Spectral-Spatial Decorrelation with 3D-SSDM:** The 3D Spatial-Spectral Decorrelation Module (3D-SSDM) reduces spectral and spatial redundancy using 3D DCT

basis functions, enabling comprehensive feature separability in complex HSI scenarios.

- **Efficient Spatial-Spectral Dependency Modeling with 3D-Mamba:** The 3D-Mamba module captures both local and global spatial-spectral dependencies, enhancing efficiency and feature interaction.
- **Robust Feature Stability with GRE:** The Global Residual Enhancement (GRE) module stabilizes feature representation, improving robustness and convergence.

The rest of this paper is organized as follows: Section 2 reviews related work, Section 3 details our approach, Section 4 presents results, Section 5 discusses model advantages, and Section 6 concludes the paper.

2. Related Work

This section reviews key approaches in hyperspectral image (HSI) classification, focusing on frequency-domain analysis, Transformer-based models, and Mamba-based models for capturing spatial-spectral dependencies.

2.1. Frequency-Domain Techniques for Image Classification

Frequency-domain techniques, including the discrete cosine transform (DCT) [19, 22, 23, 26], discrete Fourier transform (DFT) [24, 33], and wavelet transformations [32], have proven effective in enhancing feature extraction for image classification. Techniques such as Harmonic Neural Networks (HNN) [22, 23] apply 2D DCT to capture subtle variations in the frequency domain, exploiting DCT’s ability to decorrelate and concentrate energy, thereby reducing redundancy and improving classification performance in natural image classification [2]. Similarly, 2D FFT-based methods [15, 24, 33] leverage frequency information to extract discriminative features for HSI classification. WaveViT [32] utilizes discrete wavelet transformations for multi-scale feature extraction.

2.2. Mamba-Based HSI Classification Approaches

Mamba-based models present a highly promising approach for hyperspectral image (HSI) classification, focusing on capturing spatial-spectral dependencies through state-space representations. These models are particularly well-suited to the high-dimensional nature of HSI data, enabling effective feature extraction without relying on traditional convolutional or attention mechanisms. Notable Mamba-based methods, such as MiM [35], SpectralMamba [31], and WaveMamba [1], leverage state-space models to capture spatial-spectral relationships, demonstrating the potential of Mamba for HSI classification. Recent advancements, including Li et al. [13], emphasize the importance of integrating spatial and spectral features. Despite their success in modeling long-range dependencies, these approaches still

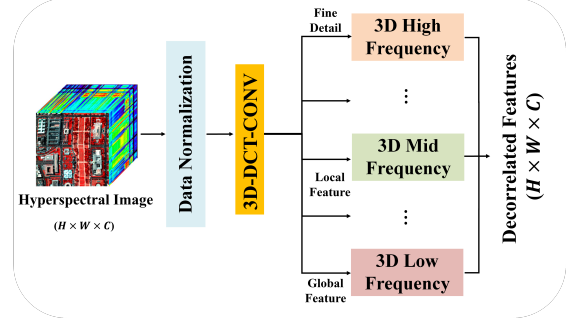


Figure 3. 3D Spatial-Spectral Decorrelation Module (3D-SSDM), applying 3D DCT basis functions to decompose the image into independent frequency components, aiding decorrelation and feature extraction.

face significant challenges related to the redundancy between spectral bands, which remains a critical gap in current Mamba-based methods.

3. Methodology

Our proposed **DCT-Mamba3D** comprises three main components, as shown in Fig. 2. First, **3D Spatial-Spectral Decorrelation Module (3D-SSDM)** applies 3D DCT basis functions to convert spatial pixels into decorrelated frequency components, reducing redundancy and isolating essential features. Second, the **3D-Mamba module** uses state-space modeling and selective scanning to capture complex spatial-spectral dependencies within the decorrelated data. Finally, the **GRE module** stabilizes feature representation across layers by integrating global context, enhancing robustness and classification accuracy.

3.1. 3D-SSDM Module

The **3D-SSDM Module** begins with a **Stem** stage for shallow feature extraction and normalization. HSIs contain hundreds of contiguous spectral bands with high inter-band correlation. To address this, 3D-SSDM applies **3D DCT basis functions** to convert spatial pixels into decorrelated frequency components across both spatial and spectral dimensions. It enhances feature clarity by consolidating most of the energy into distinct frequency components, as shown in Fig. 3.

The 3D DCT generates a set of spatial-spectral frequency components, capturing varying HSI characteristics. In a $3 \times 3 \times 3$ setup, the 3D DCT yields 27 basis functions, with low frequencies capturing smooth variations and high frequencies capturing fine-grained details.

Representing the HSI as $X \in \mathbb{R}^{H \times W \times C}$ (where H , W , and C are spatial and spectral dimensions), the 3D DCT is

applied as:

$$X_{\text{freq}}(i, j, k) = \sum_{x=0}^{H-1} \sum_{y=0}^{W-1} \sum_{z=0}^{C-1} X(x, y, z) \cdot \psi_{i,j,k}(x, y, z), \quad (1)$$

where $\psi_{i,j,k}(x, y, z)$ represents the 3D DCT basis functions, decorrelating both spatial and spectral dimensions and extracting spatial-spectral frequency features.

The basis functions $\psi_{i,j,k}(x, y, z)$ are defined as:

$$\begin{aligned} \psi_{i,j,k}(x, y, z) &= \alpha_i \alpha_j \alpha_k \cos\left(\frac{\pi(2x+1)i}{2H}\right) \\ &\times \cos\left(\frac{\pi(2y+1)j}{2W}\right) \cos\left(\frac{\pi(2z+1)k}{2C}\right), \end{aligned} \quad (2)$$

where normalization factors α_n are:

$$\alpha_n = \begin{cases} \sqrt{\frac{1}{N}} & \text{if } n = 0, \\ \sqrt{\frac{2}{N}} & \text{if } n > 0, \end{cases}$$

with N as H , W , or C .

3.2. 3D-Mamba Module

The **3D-Mamba module** employs a bidirectional state-space model (SSM) to capture spatial-spectral dependencies within the frequency-domain data X_{freq} from the 3D-SSDM. It operates directly on decorrelated data, distinguishing similar features and refining spatial-spectral information across all dimensions.

After decorrelation, the input X_{freq} undergoes the following stages:

- **Patch Embeddings:** The 3D-Mamba module decomposes X_{freq} into spatial, spectral, and residual components via specialized embedding layers in the frequency domain. This setup separates essential features and prepares data for selective scanning:

$$\begin{aligned} x_{\text{spatial}} &= F_{\text{PE}_1}(X_{\text{freq}}), & x_{\text{spectral}} &= F_{\text{PE}_2}(X_{\text{freq}}), \\ x_{\text{residual}} &= F_{\text{PE}_3}(X_{\text{freq}}). \end{aligned} \quad (3)$$

- **Frequency Spatial and Spectral bidirectional SSM:** Using SiLU activation for non-linearity, x_{spatial} and x_{spectral} undergo selective scanning within the SSM framework, capturing spatial-spectral dependencies in independent frequency components:

$$\begin{aligned} h_{\text{spatial}}(t) &= A_s \cdot s(t) + B_s \cdot \text{SiLU}(x_{\text{spatial}}(t)), \\ h_{\text{spectral}}(t) &= A_v \cdot v(t) + B_v \cdot \text{SiLU}(x_{\text{spectral}}(t)), \end{aligned} \quad (4)$$

where $s(t)$ and $v(t)$ denote latent spatial and spectral states, and $h_{\text{spatial}}(t)$, $h_{\text{spectral}}(t)$ are the outputs, enhancing independence across frequency domains.

- **Feature Aggregation and Normalization:** The outputs $h_{\text{spatial}}(t)$ and $h_{\text{spectral}}(t)$ are combined with residuals x_{residual} , and normalized for stability:

$$y_{\text{mamba}}(t) = \gamma_0 \cdot x_{\text{residual}} + \gamma_1 \cdot h_{\text{spatial}}(t) + \gamma_2 \cdot h_{\text{spectral}}(t), \quad (5)$$

where $y_{\text{mamba}}(t)$ is the final spatial-spectral feature map, combining initial decorrelated features with refined updates.

3.3. GRE Module

The **GRE module** enhances feature robustness by integrating global context with spatial-spectral features extracted by the 3D-Mamba module. By introducing a residual connection, the GRE module stabilizes training and preserves key information across layers.

The GRE module receives y_{mamba} from the 3D-Mamba module and combines it with X_{freq} from the 3D-SSDM to form the final output F_{out} :

$$F_{\text{out}} = y_{\text{mamba}} + \alpha X_{\text{freq}}, \quad (6)$$

where F_{out} is the final feature map, and α is a learnable parameter balancing contributions from y_{mamba} and X_{freq} .

The output F_{out} feeds into the classification layer, completing the feature extraction pipeline for HSI classification.

For optimization, a composite loss function is used, combining cross-entropy loss and an optional regularization term for spectral decorrelation:

$$\mathcal{L} = \mathcal{L}_{\text{CE}} + \lambda \mathcal{L}_{\text{reg}}, \quad (7)$$

where \mathcal{L}_{CE} is the cross-entropy loss, \mathcal{L}_{reg} penalizes spectral redundancy, and λ is a regularization weight.

4. Experiments

4.1. Datasets and Setup

We evaluate DCT-Mamba3D on three benchmark hyperspectral image (HSI) classification datasets: Indian Pines, Kennedy Space Center (KSC), and Houston2013, each containing diverse land cover classes with distinct spectral characteristics. The Indian Pines dataset, featuring challenges like "same object, different spectra" and "different objects, same spectra," is especially suited for analyzing our model's spectral decorrelation capabilities. All datasets are split with 10% for training and 90% for testing, and model performance is averaged over 10 runs for robustness. Evaluation metrics include overall accuracy (OA), average accuracy (AA), Kappa coefficient, and F1-score per class. Our method is compared with leading models, including 2D-CNN [28], 3D-CNN [29], HybridSN [16], ViT [6], HiT [30], MorphF [17], SSFTT [20], and MiM [35].

4.2. Spectral Correlation Heatmaps

Figure 4 shows Spearman correlation heatmaps on the Indian Pines dataset for (a) 2D-CNN, (b) HiT, and (c) DCT-Mamba3D. In each heatmap, the x- and y-axes represent spectral bands, with high off-diagonal values indicating spectral redundancy. The 2D-CNN retains substantial redundancy, HiT reduces some but maintains redundancy in adjacent bands, while DCT-Mamba3D achieves marked decorrelation, contributing to improved classification performance.

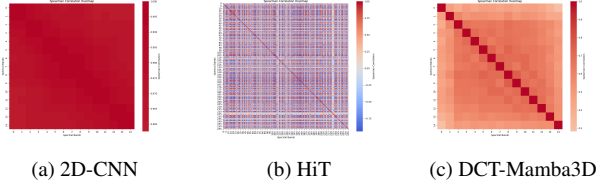


Figure 4. Spearman correlation heatmaps on the Indian Pines dataset, comparing (a) 2D-CNN, (b) HiT (Transformer-based), and (c) DCT-Mamba3D.

4.3. Classification Accuracy Comparison

We compare the classification performance of DCT-Mamba3D with leading models, including 2D-CNN, 3D-CNN, HybridSN, ViT, HiT, MorphF, SSFTT, and MiM. As shown in Table 1, DCT-Mamba3D demonstrates effective performance in hyperspectral image classification, particularly in challenging cases.

Our method demonstrates particular advantages in challenging cases: - *Same Object, Different Spectra*: For classes like Corn-notill and Corn-mintill, DCT-Mamba3D substantially improves classification accuracy, effectively capturing intra-class spectral variability. The decorrelation provided by the 3D Spectral Decorrelation Module enables the model to distinguish subtle spectral variations within similar classes, resulting in higher F1-scores for these classes. - *Different Objects, Same Spectra*: For classes such as Buildings-Grass-Trees-Drives and Stone-Steel-Towers, DCT-Mamba3D outperforms other models, highlighting its ability to reduce spectral redundancy and improve separability in classes with similar spectral characteristics.

4.3.1. t-SNE Visualization Analysis

We conducted a t-SNE visualization analysis to evaluate the effectiveness of DCT-Mamba3D in feature discrimination, as shown in Fig. 5. The results indicate that DCT-Mamba3D generates compact, well-separated clusters, demonstrating its robust capability in decorrelating complex spectral and spatial features. This enhanced decorrelation improves class separability by reducing interclass misclassification and strengthens in-class cohesion, addressing key challenges in hyperspectral imaging, such as “same ob-

ject, different spectra” and “different objects, same spectra.” By leveraging 3D-SSDM, DCT-Mamba3D effectively minimizes spectral and spatial redundancies. It results in clear and distinct feature representations, particularly beneficial in scenarios with overlapping or redundant spectral information.

4.4. Training Loss Comparison

To further demonstrate the efficiency of our proposed model, we compare the training loss curves of the DCT-Mamba3D model with those of a 2D-CNN and HiT, as shown in Figure 6. Each model’s training loss was recorded across the training iterations to analyze convergence behavior. The results clearly show that the DCT-Mamba3D model achieves a faster and more stable convergence compared to the 2D-CNN and HiT baselines.

Table 4. Ablation Study Results on the Indian Pines Dataset, showing Overall Accuracy (OA), Average Accuracy (AA), and Kappa Score for each configuration.

Configuration	OA (%)	AA (%)	Kappa (%)
3D-SDM Only	93.55	82.63	92.65
3D-MambaNet Only	94.97	85.56	94.26
No GRE	94.62	85.08	93.87
Full DCT-Mamba3D	95.23	86.81	94.55

Table 5. DCT-Mamba3D Performance on Different Datasets and Sample Sizes, showing Overall Accuracy (OA) and Kappa Score for each configuration.

Dataset	Sample Size (%)	OA (%)	Kappa (%)
Indian Pines	1%	49.58	40.68
Indian Pines	3%	77.81	74.59
Indian Pines	5%	82.79	80.21
Indian Pines	7%	86.67	84.69
Indian Pines	10%	95.23	94.55
KSC	1%	61.64	56.22
KSC	3%	78.18	75.45
KSC	5%	89.21	87.95
KSC	7%	93.54	92.80
KSC	10%	99.50	99.44
Houston2013	1%	68.75	66.17
Houston2013	3%	86.20	85.08
Houston2013	5%	92.09	91.45
Houston2013	7%	94.46	94.01
Houston2013	10%	98.15	98.00

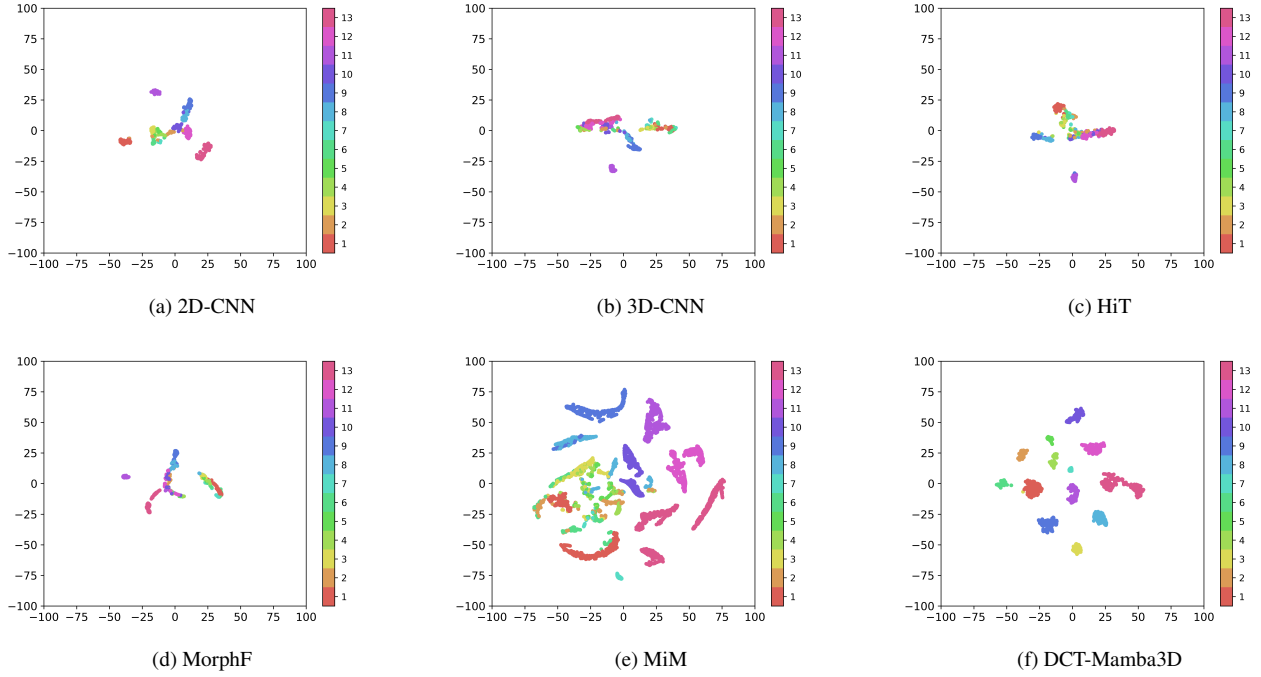


Figure 5. t-SNE visualization of feature embeddings across models on the KSC dataset.

Table 1. Classification accuracy comparison on the Indian Pines dataset with 10% training samples.

Class	2D-CNN	3D-CNN	HybridSN	ViT	HiT	MorphF	SSFTT	MiM	DCT-Mamba3D
Alfalfa	92.82	70.82	34.67	76.55	0.00	79.58	89.95	76.20	95.19
Corn-notill	93.81	89.33	88.50	94.10	91.21	93.08	92.40	92.49	95.15
Corn-mintill	92.19	87.44	81.40	93.16	89.69	90.15	88.62	89.03	93.47
Corn	97.94	94.78	83.47	99.58	84.51	92.96	96.23	93.06	99.01
Grass-pasture	93.09	92.88	84.74	91.34	45.75	95.13	93.71	93.20	94.17
Grass-trees	95.65	94.41	82.42	89.85	94.06	95.80	94.43	96.01	94.72
Grass-pasture-mowed	7.94	0.00	1.21	0.00	0.00	66.25	56.16	32.43	16.11
Hay-windrowed	99.69	99.09	92.37	99.83	100.00	99.81	99.23	99.92	99.41
Oats	73.30	0.00	0.00	0.00	0.00	9.19	38.88	53.87	44.60
Soybean-notill	87.78	83.76	82.54	89.52	81.26	89.35	87.84	86.27	80.89
Soybean-mintill	96.26	94.33	93.02	96.58	96.92	96.71	96.08	96.27	96.77
Soybean-clean	91.80	89.17	81.26	91.69	87.08	88.93	87.39	84.99	93.85
Wheat	98.12	86.12	47.40	97.28	92.43	92.52	93.27	91.09	97.83
Woods	98.28	97.96	97.28	98.20	99.74	98.87	98.88	98.04	98.51
Buildings-Grass-Trees-Drives	97.82	92.51	74.80	98.05	87.90	95.08	94.88	92.95	98.74
Stone-Steel-Towers	52.74	51.18	15.74	34.79	0.00	55.80	34.81	15.01	68.36
Accuracy (%)	94.48	91.65	86.81	94.18	88.88	94.14	93.36	92.81	95.23
Kappa (%)	93.69	90.45	84.87	93.35	87.24	93.30	92.42	91.78	94.55

Table 6. Complexity Analysis on Indian Pines Dataset

Method	FLOPS	Parameters (M)
3D-CNN	0.50	0.50
HybridSN	5.3	4.32
ViT	0.68	13.2
HiT	11.93	20.94
MorphF	0.17	0.24
SSFTT	0.24	0.93
MiM	0.50	0.18
DCT-Mamba3D	4.02	19.56

The training loss curves highlight a significant advantage of the DCT-Mamba3D model in terms of convergence speed. It achieves near-zero training loss in fewer iterations than both 2D-CNN and HiT, showcasing its efficient feature extraction and decorrelation capabilities in the frequency domain. This rapid convergence not only reduces training time but also demonstrates the robustness of the model in handling complex spatial-spectral dependencies, further supporting its effectiveness in hyperspectral image classification.

Table 2. Performance Comparison on Kennedy Space Center Dataset (10% Training Samples)

Class	2D-CNN	3D-CNN	HySN	ViT	HiT	MorphF	SSFTT	MiM	DCT-Mamba3D
Scrub	97.38	95.96	95.89	91.62	86.13	80.24	92.20	98.32	99.02
Willow swamp	95.16	87.20	87.77	74.05	98.69	57.59	88.83	93.30	98.13
Cabbage palm hammock	97.78	91.63	94.18	85.03	99.17	20.20	49.84	93.98	97.99
Cabbage palm/oak ham	92.82	83.38	89.29	93.50	98.36	52.04	82.66	74.07	99.84
Slash pine	89.94	78.78	78.63	94.89	98.83	70.67	95.07	21.99	99.94
Oak/broadleaf ham	94.68	93.27	90.85	93.21	99.74	41.96	90.31	93.72	98.72
Hardwood swamp	98.79	99.32	99.05	99.50	99.02	25.76	66.07	91.61	100.00
Graminoid marsh	94.66	97.62	96.55	89.51	96.78	67.25	85.22	99.62	98.74
Spartina marsh	97.49	99.70	99.40	95.99	99.99	73.41	81.59	99.89	99.94
Cattail marsh	97.17	97.37	98.36	97.75	99.03	89.24	100.00	100.00	99.98
Salt marsh	99.65	99.98	98.06	100.00	100.00	97.67	98.28	100.00	100.00
Mud flats	98.28	97.85	99.08	99.65	99.17	95.03	100.00	100.00	100.00
Water	100.00	100.00	100.00	100.00	99.86	100.00	100.00	100.00	100.00
Accuracy (%)	97.31	95.99	96.28	94.77	95.51	80.36	91.99	95.80	99.50
Kappa (%)	97.01	95.54	95.86	94.16	95.03	77.82	91.02	95.32	99.44

Table 3. Comparison with Leading Transformer and Mamba Models on Houston2013 Dataset (10% Training Samples)

Class	2D-CNN	3D-CNN	HybridSN	ViT	HiT	MorphF	SSFTT	MiM	DCT-Mamba3D
Unclassified	95.45	93.10	92.46	93.45	94.63	93.78	90.18	93.36	96.60
Healthy Grass	96.45	90.56	88.22	87.16	90.15	94.20	92.70	95.09	97.78
Stressed Grass	99.32	97.35	97.84	97.29	98.93	99.18	99.52	99.03	98.89
Synthetic Grass	92.42	89.78	81.79	85.45	87.57	97.76	93.53	91.13	96.54
Soil	99.57	97.53	97.47	99.56	99.66	99.74	99.33	99.90	99.30
Water	95.02	86.73	93.09	90.34	88.05	94.86	93.44	91.60	93.01
Residential	93.96	86.51	86.07	89.16	90.17	97.10	95.40	90.88	98.10
Commercial	96.59	89.12	92.09	96.86	96.95	98.21	96.59	99.39	97.38
Road	94.59	84.52	76.40	90.09	89.77	96.95	95.06	93.98	97.42
Highway	97.30	94.23	94.67	99.17	97.88	99.20	99.22	99.73	99.90
Railway	99.41	87.33	82.52	98.29	99.50	99.85	99.56	98.10	99.96
Parking Lot 1	97.78	95.51	96.37	98.04	98.54	99.45	98.21	99.24	99.17
Parking Lot 2	96.27	88.31	87.86	94.16	94.78	97.38	97.69	96.77	96.94
Tennis Court	99.92	98.84	96.61	99.85	99.95	99.87	99.51	99.78	99.85
Running Track	98.92	95.49	94.23	96.77	98.75	98.96	99.15	98.81	98.58
Accuracy (%)	96.66	91.36	90.09	94.09	94.87	97.75	96.37	96.32	98.15
Kappa (%)	96.39	90.65	89.29	93.61	94.45	97.57	96.08	96.02	98.00

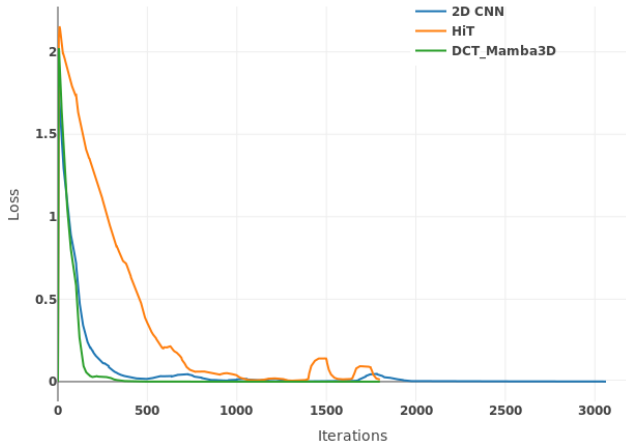


Figure 6. Training loss comparison between 2D-CNN, HiT, and the DCT-Mamba3D model.

4.5. Ablation Study and Complexity Analysis

We conducted an ablation study to evaluate the contributions of key components in the DCT-Mamba3D model.

Three configurations were tested:

1. *3D-SDM Only*: Excludes the 3D-MambaNet, focusing on spectral decorrelation, achieving OA of 93.55%, AA of 82.63%, and Kappa score of 92.65%.
2. *3D-MambaNet Only*: Excludes the 3D-SDM, focusing on spatial feature extraction, achieving OA of 94.97%, AA of 85.56%, and Kappa score of 94.26%.
3. *No GRE (Global Residual Enhancement)*: Excludes the GRE, achieving OA of 94.62%, AA of 85.08%, and Kappa score of 93.87%.

Table 4 summarizes the OA, AA, and Kappa scores for each configuration, alongside the full DCT-Mamba3D model. The results highlight the model’s integrated spatial-spectral feature extraction advantage, particularly for “same object, different spectra” and “different objects, same spectra” cases.

To further examine DCT-Mamba3D’s performance, we evaluated it on the Indian Pines, KSC, and Houston2013 datasets with varying training sample sizes, particularly under limited training samples, as shown in Table 5. The results indicate that DCT-Mamba3D maintains high OA

and Kappa scores even with limited samples (e.g., 1% and 3%), underscoring its robust feature extraction capabilities. This effectiveness can be attributed to the 3D-SSDM’s spectral-spatial decorrelation, which reduces redundancy and enhances feature separability. As sample size increases, the model consistently improves in both OA and Kappa, demonstrating its scalability and robustness across varying data conditions, making it particularly suitable for challenging HSI classification tasks.

4.5.1. Complexity Analysis

We evaluated the computational complexity of DCT-Mamba3D relative to baseline models on the Indian Pines dataset, as detailed in Table 6, focusing on FLOPS and parameter counts. While DCT-Mamba3D incurs a higher computational cost than CNN models, this is offset by substantial performance gains. Compared to other Mamba-based architectures, such as MiM, DCT-Mamba3D demonstrates an optimized balance of complexity, accuracy, and decorrelation effectiveness, making it well-suited for applications requiring both precision and computational efficiency.

5. Discussion

Our **DCT-Mamba3D** model addresses HSI classification challenges by leveraging spectral-spatial decorrelation and effective feature extraction through its integrated modules: **3D-SSDM**, **3D-Mamba**, and **GRE**.

3D-SSDM for Spectral Decorrelation and Feature Extraction: Using 3D DCT basis functions, 3D-SSDM reduces spectral and spatial redundancy while extracting critical features across dimensions. Its enhanced decorrelation improves the model’s ability to manage cases of high spectral similarity, such as in ‘different objects, same spectra’ scenarios. Ablation studies show that the 3D-SSDM alone achieves competitive accuracy, underscoring its effectiveness in isolating relevant features.

3D-Mamba for Enhanced Spatial-Spectral Dependencies: 3D-Mamba effectively captures spatial-spectral dependencies through bidirectional state-space layers, particularly aiding in differentiating subtle spectral variations, as in ‘same object, different spectra’ scenarios. This structure balances complexity while maintaining efficient feature interaction across spatial and spectral dimensions.

GRE for Stability and Robust Training: GRE integrates residual spatial-spectral features, stabilizing feature representation across layers. This stability accelerates convergence, contributing to DCT-Mamba3D’s efficient training times and robustness during learning, despite its complex architecture.

Performance with Limited Data and Complexity Efficiency: DCT-Mamba3D demonstrates strong feature discrimination even with limited training data, achieving high

accuracy and Kappa scores at smaller sample sizes. Its balanced computational complexity, as shown in Table 6, allows for superior accuracy compared to other models, with manageable FLOPS and parameter counts, making it suitable for resource-constrained applications.

6. Conclusion

In this paper, we proposed **DCT-Mamba3D**, a framework for hyperspectral image (HSI) classification designed to address spectral redundancy and complex spatial-spectral dependencies. The architecture integrates three core modules: a **3D Spatial-Spectral Decorrelation Module (3D-SSDM)** that utilizes a 3D DCT basis functions to reduce redundancy and enhance feature clarity; a **3D-Mamba module** that captures intricate spatial-spectral relationships through a bidirectional state-space model; and a **Global Residual Enhancement (GRE) module** to stabilize feature representation for improved robustness and convergence. Our experiments on benchmark HSI datasets demonstrated that DCT-Mamba3D surpasses state-of-the-art methods, particularly in challenging scenarios with high spectral similarity or spectral variability.

Future Work: Future improvements could focus on exploring adaptive frequency selection to further enhance the generalizability of DCT-Mamba3D across diverse HSI datasets, potentially making it more robust to varying data characteristics and environmental conditions.

References

- [1] Muhammad Ahmad, Muhammad Usama, and Manual Mazzara. Wavemamba: Spatial-spectral wavelet mamba for hyperspectral image classification. *arXiv preprint arXiv:2408.01231*, 2024. 2, 3
- [2] Nasir Ahmed, T. Natarajan, and Kamisetty R Rao. Discrete cosine transform. *IEEE Transactions on Computers*, 100(1): 90–93, 1974. 3
- [3] Mohamed Amine Bendoumi, Mingyi He, and Shaohui Mei. Hyperspectral image resolution enhancement using high-resolution multispectral image based on spectral unmixing. *IEEE Transactions on Geoscience and Remote Sensing*, 52(10):6574–6583, 2014. 2
- [4] Yushi Chen, Hanlu Jiang, Chunyang Li, Xiuping Jia, and Pedram Ghamisi. Deep feature extraction and classification of hyperspectral images based on convolutional neural networks. *IEEE Transactions on Geoscience and Remote Sensing*, 54(10):6232–6251, 2016. 2
- [5] Shang-Qi Deng, Liang-Jian Deng, Xiao Wu, Ran Ran, Danfeng Hong, and Gemine Vivone. Psrt: Pyramid shuffle-and-reshuffle transformer for multispectral and hyperspectral image fusion. *IEEE Transactions on Geoscience and Remote Sensing*, 61:1–15, 2023. 1
- [6] Alexey Dosovitskiy, Lucas Beyer, Alexander Kolesnikov, Dirk Weissenborn, Xiaohua Zhai, Thomas Unterthiner,

- Mostafa Dehghani, Matthias Minderer, Georg Heigold, Sylvain Gelly, et al. An image is worth 16x16 words: Transformers for image recognition at scale. *arXiv preprint arXiv:2010.11929*, 2020. 2, 4
- [7] Jiaqi Feng, Qixiong Wang, Guangyun Zhang, Xiuping Jia, and Jihao Yin. Cat: Center attention transformer with stratified spatial-spectral token for hyperspectral image classification. *IEEE Transactions on Geoscience and Remote Sensing*, 2024. 2
- [8] Lin He, Jun Li, Chenying Liu, and Shutao Li. Recent advances on spectral-spatial hyperspectral image classification: An overview and new guidelines. *IEEE Transactions on Geoscience and Remote Sensing*, 56(3):1579–1597, 2017. 1
- [9] Danfeng Hong, Bing Zhang, Xuyang Li, Yuxuan Li, Chenyu Li, Jing Yao, Naoto Yokoya, Hao Li, Pedram Ghamisi, Xiuping Jia, et al. Spectralgpt: Spectral remote sensing foundation model. *IEEE Transactions on Pattern Analysis and Machine Intelligence*, 2024. 2
- [10] Sen Jia, Jianhui Liao, Meng Xu, Yan Li, Jiasong Zhu, Weiwei Sun, Xiuping Jia, and Qingquan Li. 3D Gabor convolutional neural network for hyperspectral image classification. *IEEE Transactions on Geoscience and Remote Sensing*, 60:1–16, 2022. 2
- [11] Jun Li, José M Bioucas-Dias, and Antonio Plaza. Spectral-spatial hyperspectral image segmentation using subspace multinomial logistic regression and markov random fields. *IEEE Transactions on Geoscience and Remote Sensing*, 50(3):809–823, 2012. 1
- [12] Miaoyu Li, Ying Fu, Tao Zhang, Ji Liu, Dejing Dou, Chenggang Yan, and Yulun Zhang. Latent diffusion enhanced rectangle transformer for hyperspectral image restoration. *IEEE Transactions on Pattern Analysis and Machine Intelligence*, 2024. 1
- [13] Yapeng Li, Yong Luo, Lefei Zhang, Zengmao Wang, and Bo Du. Mambahi: Spatial-spectral mamba for hyperspectral image classification. *IEEE Transactions on Geoscience and Remote Sensing*, 2024. 3
- [14] Matteo E Paoletti, Jean M Haut, Javier Plaza, and Antonio Plaza. Deep learning classifiers for hyperspectral imaging: A review. *ISPRS Journal of Photogrammetry and Remote Sensing*, 158:279–317, 2019. 1
- [15] Xin Qiao and Weimin Huang. A dual frequency transformer network for hyperspectral image classification. *IEEE Journal of Selected Topics in Applied Earth Observations and Remote Sensing*, pages 1–12, 2023. 2, 3
- [16] Swapnil Karun Roy, Gopal Krishna, and Shiv Ram Dubey. HybridSN: Exploring 3D-2D CNN Feature Hierarchy for Hyperspectral Image Classification. *IEEE Geoscience and Remote Sensing Letters*, 17(2):277–281, 2020. 2, 4
- [17] Soumya Kanti Roy, Akash Deria, Chirag Shah, Jean-Marc Haut, Qian Du, and Antonio Plaza. Spectral-spatial morphological attention transformer for hyperspectral image classification. *IEEE Transactions on Geoscience and Remote Sensing*, 61:1–15, 2023. 2, 4
- [18] Linus Scheibenreif, Michael Mommert, and Damian Borth. Masked vision transformers for hyperspectral image classification. In *Proceedings of the IEEE/CVF conference on computer vision and pattern recognition*, pages 2166–2176, 2023. 2
- [19] Xing Shen, Jirui Yang, Chunbo Wei, Bing Deng, Jianqiang Huang, Xian-Sheng Hua, Xiaoliang Cheng, and Kewei Liang. Dct-mask: Discrete cosine transform mask representation for instance segmentation. In *Proceedings of the IEEE/CVF conference on computer vision and pattern recognition*, pages 8720–8729, 2021. 2, 3
- [20] Liang Sun, Guangming Zhao, Yisong Zheng, and Zuxin Wu. Spectral-spatial feature tokenization transformer for hyperspectral image classification. *IEEE Transactions on Geoscience and Remote Sensing*, 60:1–14, 2022. 4
- [21] James Theiler, Amanda Ziemann, Stefania Matteoli, and Marco Diani. Spectral variability of remotely sensed target materials: Causes, models, and strategies for mitigation and robust exploitation. *IEEE Geoscience and Remote Sensing Magazine*, 7(2):8–30, 2019. 1, 2
- [22] Matej Ulicny, Vladimir A Krylov, and Rozenn Dahyot. Harmonic networks for image classification. 2019. 2, 3
- [23] Matej Ulicny, Vladimir A Krylov, and Rozenn Dahyot. Harmonic convolutional networks based on discrete cosine transform. *Pattern Recognition*, 129:108707, 2022. 2, 3
- [24] Ke Wang, Bin Yong, and Zhaohui Xue. Frequency domain-based features for hyperspectral image classification. *IEEE Geoscience and Remote Sensing Letters*, 16(9):1417–1421, 2019. 3
- [25] Jingran Xu, Jiankang Zhao, and Yuchao Fu. An efficient hyperspectral image classification method using deep fusion of 3D discrete wavelet transform and CNN. *IEEE Geoscience and Remote Sensing Letters*, 20:1–5, 2023. 2
- [26] Kai Xu, Minghai Qin, Fei Sun, Yuhao Wang, Yen-Kuang Chen, and Fengbo Ren. Learning in the frequency domain. In *Proceedings of the IEEE/CVF conference on computer vision and pattern recognition*, pages 1740–1749, 2020. 2, 3
- [27] Muge Yan, Lizhi Wang, Lin Zhu, and Hua Huang. Exploiting frequency correlation for hyperspectral image reconstruction. *arXiv preprint arXiv:2406.00683*, 2024. 2
- [28] Xiaofei Yang, Yunming Ye, Xutao Li, Raymond YK Lau, Xiaofeng Zhang, and Xiaohui Huang. Hyperspectral image classification with deep learning models. *IEEE Transactions on Geoscience and Remote Sensing*, 56(9):5408–5423, 2018. 2, 4
- [29] Xiaofei Yang, Xin Zhang, Yun Ye, Raymond Y Lau, Sheng Lu, Xin Li, and Xiaodong Huang. Synergistic 2D/3D convolutional neural network for hyperspectral image classification. *Remote Sensing*, 12(12):2033, 2020. 2, 4
- [30] Xiaofei Yang, Weijia Cao, Yanan Lu, and Yicong Zhou. Hyperspectral image transformer classification networks. *IEEE Transactions on Geoscience and Remote Sensing*, 60:1–15, 2022. 2, 4
- [31] Jing Yao, Danfeng Hong, Chenyu Li, and Jocelyn Chanussot. Spectralmamba: Efficient mamba for hyperspectral image classification. *arXiv preprint arXiv:2404.08489*, 2024. 1, 2, 3
- [32] Ting Yao, Yingwei Pan, Yehao Li, Chong-Wah Ngo, and Tao Mei. Wave-vit: Unifying wavelet and transformers for visual representation learning. In *European Conference on Computer Vision*, pages 328–345. Springer, 2022. 3

- [33] Jun Zhang, Cheng Zhang, Shuai Liu, Zhenwei Shi, and Bin Pan. Three-dimensional frequency domain transform network for cross-scene hyperspectral image classification. *IEEE Transactions on Geoscience and Remote Sensing*, 2024. [3](#)
- [34] Liangpei Zhang, Lefei Zhang, and Bo Du. Deep learning for remote sensing data: A technical tutorial on the state of the art. *IEEE Geoscience and Remote Sensing Magazine*, 4(2): 22–40, 2016. [1](#)
- [35] Weilian Zhou, Sei-Ichiro Kamata, Haipeng Wang, Man Sing Wong, and Huiying Cynthia Hou. Mamba-in-Mamba: Centralized Mamba-Cross-Scan in Tokenized Mamba model for hyperspectral image classification. *Neurocomputing*, page 128751, 2024. [2](#), [3](#), [4](#)
- [36] Lianghui Zhu, Bencheng Liao, Qian Zhang, Xinlong Wang, Wenyu Liu, and Xinggang Wang. Vision mamba: Efficient visual representation learning with bidirectional state space model. *arXiv preprint arXiv:2401.09417*, 2024. [2](#)